How to Look for Compounds: Predictive Screening and in situ Studies in Na–Zn–Bi System

Volodymyr Gvozdetskyi,[a] Renhai Wang,[b, c] Weiyi Xia,[d] Feng Zhang,[e] Zijing Lin,[c] Kai-Ming Ho,[d] Gordon Miller,[a] and Julia V. Zaikina*[a]

Abstract: Here, the combination of theoretical computations followed by rapid experimental screening and in situ diffraction studies is demonstrated as a powerful strategy for novel compounds discovery. When applied for the previously "empty" Na–Zn–Bi system, such an approach led to four novel phases. The compositional space of this system was rapidly screened via the hydride route method and the theoretically predicted NaZnBi (PbClF type, *P*4/*nmm*) and $Na_{11}Zn_2Bi_5$ ($Na_{11}Cd_2Sb_5$ type, $P\bar{1}$) phases were successfully synthesized, while other computationally generated compounds on the list were rejected. In addition, single crystal X-ray diffraction studies of NaZnBi indicate minor deviations from the stoichiometric 1:1:1 molar ratio. As a result, two isostructural (PbClF type, *P*4/*nmm*) Zn-deficient phases with similar compositions, but distinctly different unit cell parameters were discovered. The vacancies on Zn sites and unit cell expansion were rationalized from bonding analysis using electronic structure calculations on stoichiometric "NaZnBi". *In-situ* synchrotron powder X-ray diffraction studies shed light on complex equilibria in the Na–Zn–Bi system at elevated temperatures. In particular, the high-temperature polymorph *HT*-Na_3Bi (BiF_3 type, $Fm\bar{3}m$) was obtained as a product of $Na_{11}Zn_2Bi_5$ decomposition above 611 K. *HT*-Na_3Bi cannot be stabilized at room temperature by quenching, and this type of structure was earlier observed in the high-pressure polymorph *HP*-Na_3Bi above 0.5 GPa. The aforementioned approach of predictive synthesis can be extended to other multinary systems.

Introduction

Traditionally, novel compounds have been discovered serendipitously. As capabilities of experimental laboratories have grown, numerous compounds have been synthesized, investigated, and compiled in various databases: Inorganic Crystal Structure Database (ICSD),[1] Cambridge Structural Database (CSD),[2] Pearson's Crystal Data,[3] and Pauling File.[4] On the other hand, computational resources have also developed considerably in the last decades, resulting in many different approaches to predict new stable compounds: random structure searching, simulated annealing, evolutionary algorithms, and particle swarm optimization.[5–9] As a result, numerous depositories with theoretically predicted compounds also emerged, including Open Quantum Materials Database,[10] Materials Project,[11] AFLOW library,[12] Electronic Structure Project,[13] and Computational Materials Repository.[14] With all of the theoretically predicted compounds, the question of experimental validation naturally arises. High-throughput computations combined with an appropriate experimental method can promote an effective screening strategy for new phases. This way, the discovery of materials can be refocused from traditional "exploratory" into a more targeted approach.[15–21]

An accurate, rapid, and reliable method suitable for experimental verification of theoretically predicted compounds containing alkali or alkaline-earth elements is the synthetic hydride route.[22–35] This method utilizes salt-like hydrides (instead of ductile metals) that can be ball-milled into homogeneous mixture of precursors. Significant advantages include short reaction times and excellent compositional control over target phases obtained with high yield and purity. This method has been successfully applied to prepare several complex materials, including ternary borides, antimonides, arsenides, silicides, and germanides, where comprehensive control over composition is crucial for the targeted preparation

[a] Dr. V. Gvozdetskyi, Prof. G. Miller, Prof. J. V. Zaikina
Department of Chemistry
Iowa State University
Ames, Iowa 50011 (United States of Amerika)
E-mail: yzaikina@iastate.edu
[b] Dr. R. Wang
School of Physics and Optoelectronic Engineering
Guangdong University of Technology
Guangzhou 510006 (China)
[c] Dr. R. Wang, Prof. Z. Lin
Department of Physics
University of Science and Technology of China
Hefei 230026 (China)
[d] Dr. W. Xia, Prof. K.-M. Ho
Department of Physics and Astronomy
Iowa State University
Ames, Iowa 50011 (United States of Amerika)
[e] Dr. F. Zhang
Ames Laboratory
U.S. Department of Energy
Ames, Iowa 50011 (United States of Amerika)

Supporting information for this article is available on the WWW under https://doi.org/10.1002/chem.202101948

of compositionally similar compounds.[27–35] In particular, the hydride route in tandem with computational predictions from an adaptive genetic algorithm (AGA)[36–40] search led to the discovery of layered LiNiB polymorphs.[31] The highly efficient and adaptive manner of AGA for theoretical predictions, together with the accuracy and "fast compositional screening" capabilities of the hydride route as experimental validation, has the potential to accelerate materials discovery. In addition, in situ powder diffraction is another powerful tool complementary to this theoretical-experimental approach for compound discovery. Variable temperature studies can further broaden the scope of investigation by shedding light on complex phase transformations at elevated temperatures, elucidating the existence of new metastable compounds, and helping to optimize synthetic conditions (temperature, concentration, duration).[34,41–43]

The ternary systems *A*-Zn-*Pn* (*A* = alkali, alkaline-earth metal, *Pn* = pnictogen) have been poorly explored due to their synthetic challenges, such as inadequate mixing of the reactant elements due to the ductility of alkali metals and high vapor pressures of zinc and alkali metals at elevated temperatures, resulting in inhomogeneous samples. Therefore, *A*-Zn-*Pn* systems are excellent candidates to apply a search for new compounds using the updated strategy. For instance, only one phase in the Na-Zn-Sb system was listed in the databases,[1–3] but 5 new ternary compounds were discovered after the fast screening with the hydride route.[33–35] High thermoelectric efficiencies identified in related ternary antimonides $Yb_{14}MnSb_{11}$,[44,45] $AeZn_2Sb_2$ (*Ae* = Ca, Sr, Ba)[46,47] and $Ca_{9-y}Eu_yZn_{4+x}Sb_9$,[48] and the discovery of *AeMPn* (*M* = Mn, Ag, Zn, Cd, *Pn* = Sb, Bi)[49,50] topological materials promotes interest in studying structure-property relationships in other *A-M-Pn* phases. Herein, we report on three new ternary compounds in the Na–Zn–Bi system, where no experimental or theoretically predicted ternary compounds have been previously reported. We use the combination of predictive theoretical calculations about the stabilities and structures of the ternary compounds followed by experimental validation using hydride synthesis and in situ powder X-ray diffraction.

Experimental

Synthesis

Starting materials for synthesis were used as received: sodium hydride (Sigma-Aldrich, 95%), sodium metal (Alfa Aesar, 99.95%), zinc powder (Alfa Aesar, 99.996%), and bismuth chunks (Alfa Aesar, 99.9%). Bismuth powders were prepared by ball-milling bismuth chunk for 12 min in an ambient atmosphere using a standard grinding set with tungsten carbide inserts and high-energy ball-mill SPEX 8000 M MIXER/MILL. All manipulations of reagents and samples were carried out under an inert argon atmosphere ($p(O_2) <$ 1 ppm, $p(H_2O) < 1$ ppm) in a glove box (LC-Technology).

Hydride route. For phase screening, powders of sodium hydride, zinc, and bismuth were weighed in various molar ratios (total mass ~0.3 g) and loaded into a polycarbonate grinding set with a methacrylate grinding ball. The vials were further sealed in plastic bags under argon atmosphere, and removed from the glovebox for ball-milling. Samples were ball-milled for 6 min to achieve sufficient mixing, longer ball-milling caused partial decomposition of NaH. Inside the glovebox, fine powders were loaded into tantalum containers, which were placed into silica reactors equipped with Swagelok safety check valves to prevent over-pressurizing of the reactors due to hydrogen gas release during the heat treatment. The reactors were evacuated to 4×10^{-5} Bar and placed into a resistance furnace (Thermo Scientific Thermolyne Type FD1500 M) equipped with a temperature controller (Eurotherm 3216). Samples for phase screening were typically heated (1.4 K/min) from room temperature to 723 K, held at that temperature for 8 h, and cooled to room temperature naturally by switching off the furnace. This temperature profile proved to be suitable to prepare $NaZn_{1-x}Bi$ and $NaZn_{1-y}Bi$ phases. In the case of $Na_{11}Zn_2Bi_5$, samples were heated (1.6 K/min) to 573 K, held there for 48 h, and cooled to room temperature by switching off the furnace. All compounds were found to be air- and moisture-sensitive, and were stored in the glovebox.

Synthesis from elements: single crystal growth. To obtain crystals suitable for single crystal X-ray diffraction experiments, a modified heating profile with a slow cooling step was employed. For $NaZn_{1-x}Bi$, elemental precursors were weighed in 1:1:1 and 1.5:1:1 molar ratios, and heated from room temperature to 843 K at a rate of 1.8 K/min, held at that temperature for 2 h, slowly cooled to 673 K at a rate of 0.015 K/min, and quenched in cold water. For $Na_{11}Zn_2Bi_5$, samples were heated from room temperature to 673 K at a rate of 1.6 K/min, held at that temperature for 8 h, slowly cooled to 473 K at a rate of 0.015 K/min, and further cooled naturally by switching off the furnace. Single crystals of the target phases were mechanically separated for further examination.

Characterization

Laboratory Powder X-ray Diffraction (PXRD). The purity of polycrystalline samples was checked using a Rigaku MiniFlex600 powder diffractometer with Cu $K\alpha$ radiation ($\lambda = 1.540593$ Å) and Ni-K_β filter. Data were collected at room temperature using a holder for air-sensitive samples. Phase analysis was performed using the PDF-2 database incorporated into the PDXL program software.[51]

Single-Crystal X-ray Diffraction (SC-XRD). Single crystal data were collected by means of a Bruker D8 VENTURE diffractometer (Photon CMOS detector, Mo–IμS microsource and Oxford Cryosystem 800 low temperature device) at 100 K. Data integration, absorption correction, and unit cell determination were performed using the APEX 3 software.[52] Starting atomic parameters were obtained by direct methods with SHELXS-2017.[53] Subsequently, the structures were refined using SHELXL-2017 (full-matrix least-squares on F_o^2).[53] Crystal structures were visualized using the program VESTA 3.[54]

Analysis of the diffraction data of $NaZn_{1-x}Bi$ revealed tetragonal symmetry ($a = 4.3131(7)$ Å, $c = 7.096(1)$ Å). The systematic absences and the *E*-value statistics indicated two possible centrosymmetric space groups: *P*4/*n* or *P*4/*nmm*. Both structure solutions imply Bi, Zn, and Na atoms occupying 2*c*, 2*a*, and 2*c* sites, respectively, so the higher symmetry space group *P*4/*nmm* was considered. Further refinements indicated partial occupancy of Zn atoms in the 2*a* site, ranging between 95.8(5) and 93.1(5) %). In total, six different single crystals were measured for consistency: three from the sample with 1:1:1 loading molar ratio and three from the sample with 1.5:1:1 loading molar ratio of Na:Zn:Bi. Details of data collections and refinements are listed in Table S1–S2, atomic coordinates and ADPs are given in Table S3.

Analysis of the diffraction data of $Na_{11-z}Zn_2Bi_5$ revealed triclinic symmetry ($a = 9.0416(5)$ Å, $b = 10.8368(6)$ Å, $c = 11.6206(7)$ Å, $\alpha = 103.461(2)^\circ$, $\beta = 97.012(2)^\circ$, $\gamma = 107.507(2)^\circ$) and centrosymmetric

space group $P\bar{1}$. Bi atoms were found to occupy five 2*i* sites, Zn in two 2*i* sites, and Na in eleven 2*i* sites. Further refinement revealed a large electron density peak in the difference Fourier map located close to the Bi(5) atomic site (7 e) and two smaller peaks (2.7 e), each near Zn(1) and Zn(2) sites. Therefore, a split-site model was considered, where the sum of site occupancy fractions (s.o.f.) for an atomic site and its split counterpart was constrained to 1, while the atomic displacement parameters (APDs) were constrained to be equal. In this refinement, three 2*i*–2*i* split positions were introduced: Bi(5)-Bi(6), Zn(1)-Zn(3), and Zn(2)-Zn(4). When Zn(3) and Zn(4) atoms are present, the adjacent Na(2) position should be vacant to avoid unrealistically short interatomic distances of 1.8-1.9 Å. When refined independently, the site occupancies of Bi(5), Zn(1), Zn(2), and Na(2) are found to be very similar: 0.975(6), 0.971(6), 0.970(1), and 0.964(8), respectively. Therefore, during the last refinement cycle these variables were constrained to be the same, leading to the following s.o.f.: Bi(5)/Bi(6) = Zn(1)/Zn(3) = Zn(2)/Zn(4) = Na(2)/vacancy = 0.9703/0.0297(5), and resulting in the formula $Na_{11-z}Zn_2Bi_5$, $z = 0.0297(5)$. Details of the data collection and refinement are summarized in Table S4, atomic coordinates and ADPs are given in Table S5.

Deposition Numbers 2086704 (for $NaZn_{0.958(5)}Bi$), 2086706 (for $NaZn_{0.949(5)}Bi$), 2086705 (for $NaZn_{0.948(6)}Bi$), 2086709 (for $NaZn_{0.942(6)}Bi$), 2086708 (for $NaZn_{0.938(5)}Bi$), 2086707 (for $NaZn_{0.931(5)}Bi$), 2086710 (for $Na_{10.9703(5)}Zn_2Bi_5$) contain the supplementary crystallographic data for this paper. These data are provided free of charge by the joint Cambridge Crystallographic Data Centre and Fachinformationszentrum Karlsruhe Access Structures service.

In Situ *Synchrotron Powder X-ray Diffraction*. High-temperature synchrotron powder X-ray diffraction data (HT-PXRD) were collected at beamline 17-BM (APS ANL) with an average wavelength $\lambda =$ 0.24158 Å. Powdered samples were loaded into 0.7 mm outer diameter thick-walled (0.1 mm) silica capillaries and sealed under vacuum. The capillaries were mounted into secondary shield capillaries (0.9 mm inner diameter and 1.1. mm outer diameter) located on a sample stage equipped with two resistive microheaters and a thermocouple set as close as possible to the measurement area. Further details of the experimental setup can be found in the literature.[55] The data were collected during heating and cooling in the temperature range 298 K→820 K→298 K with variable heating and cooling rates ~10–20 $K \cdot min^{-1}$.

Diffraction patterns were analyzed by the Rietveld refinement method using the GSAS II software package.[56] Profile parameters, background parameters, zero correction, and cell parameters were refined first. The background was fitted using a 24-point linear interpolation function, and a pseudo-Voigt function was applied to generate the profile shape. The NaZnBi structure model (PbClF type, *P*4/*nmm*) obtained from the single crystal X-ray diffraction refinement, was refined using 17-BM PXRD data (NaH:Zn:Bi sample), resulting in a satisfactory fit ($R_B = 0.09$) (Tables S6, Figure S1). Structure refinement of *HT*-Na_3Bi was performed using the structure of *HP*-Na_3Bi as an initial model (BiF_3 type, $Fm\bar{3}m$) [57]), and resulted in a good fit to the experimental pattern ($R_B = 0.05$) (Tables S7, Figure S2).

Combustion analysis. Combustion analysis was performed to obtain hydrogen content within the $NaZn_{1-y}Bi$ sample. Results (%C, %H, % N) were acquired using a PE 2100 Series II combustion analyzer (Perkin Elmer Inc., Waltham, MA) with acetanilide as a calibration standard and the combustion and reduction temperatures of 1198 and 913 K, respectively. All standards and reagents were from Perkin Elmer and/or Elementar America's Inc. The determined H content is < 0.03 wt.%, which is within the precision and accuracy of the measurement, thus no significant amount of H is present in the $NaZn_{1-y}Bi$ phase.

Computational details. First-principles calculations were carried out based on density functional theory (DFT) using VASP code.[58,59] The projected augmented-wave (PAW)[60] method was used to describe the electron-ion interaction, and the generalized gradient approximation (GGA) in the Predew-Burke-Ernzerhof (PBE)[61,62] form was employed for the exchange-correlation energy functional. A plane-wave basis with a kinetic energy cutoff of 520 eV was used. Monkhorst-Pack's sampling scheme was adopted for Brillouin zone sampling with a *k*-point grid of $2\pi \times 0.033$ $Å^{-1}$.[63] All atoms in the calculation cell were allowed to relax until the forces on each atom are smaller than 0.01 eV/Å. To characterize the thermodynamical stability, the formation energy of any given structure $Na_mZn_nBi_p$ was calculated using cubic ($Im\bar{3}m$) Na, hexagonal ($P6_3/mmc$) Zn and rhombohedral ($R\bar{3}m$) Bi, i.e. $E_f(Na_mZn_nBi_p) = [E(Na_mZn_nBi_p) - m \cdot E(Na) - n \cdot E(Zn) - p \cdot E(Bi)]/(m+n+p)$. Crystal orbital Hamilton population (COHP) curves for different interatomic contacts in stoichiometric "NaZnBi" were extracted from VASP results by using LOBSTER code.[64,65] To compare these results with a tight-binding approach, COHP and DOS curves of "NaZnBi" were calculated using the tight-binding, linear muffin-tin orbital (TB-LMTO) method in the atomic spheres approximation (ASA) by the Stuttgart code.[66–69] Exchange and correlation were treated in the local density approximation.[70] All relativistic effects except spin-orbit coupling were taken into account using a scalar relativistic approximation.[71] In the ASA, space is filled with small, overlapping Wigner-Seitz (WS) spheres at each atomic site. The symmetry of the potential is considered to be spherical inside each WS sphere, and a combined correction takes into account the overlapping part.[72] The radii of the WS spheres were obtained by requiring that the overlapping potential be the best possible approximation to the full potential, and were determined by an automatic procedure.[72] No empty spheres were needed to satisfy the LMTO volume criterion. The corresponding WS radii for the various atoms are: Na, 2.015 Å; Zn, 1.526 Å; and Al, 1.833 Å. The basis set included Na 3*s*, 3*p*, and 3*d* orbitals (3*p*, 3*d* downfolded), Zn 4*s*, 4*p*, and 3*d* orbitals, and Bi 6*s*, 6*p*, 6*d* and 5*f* orbitals (6*d*, 5*f* downfolded). The *k*-space integrations were accomplished by the tetrahedron method.[73] The self-consistent charge density was obtained using 385 irreducible k-points in the Brillouin zone.

Results and Discussion

Predictive theoretical search for ternary compounds

In contrast to the Na-Zn-Sb system, where 6 ternary compounds have been reported,[1–3,33–35] no ternary compounds have been reported in the Na–Zn–Bi system.[1–3] Binary Na-Zn and Na-Bi systems together contain only 3 known compounds: $NaZn_{13}$ ($NaZn_{13}$ type, $Fm\bar{3}c$), NaBi (CuAu, *P*4/*mmm*), and Na_3Bi (Na_3As, $P6_3/mmc$). Interestingly, no compounds have been reported in the binary Zn–Bi system. This is again in contrast to the Zn-Sb system, where several binary compounds exist: Zn_4Sb_3, $Zn_{13}Sb_{10}$, Zn_8Sb_7, Zn_3Sb_2, ZnSb).[74–78] The paucity of bismuthides may originate from the larger atomic size differences between Zn and Bi, making these structures less stable, or could be due to the lack of effective hybridization between the Bi and Zn valence orbitals, or might be solely due to the synthetic difficulties. It should be noted that Bi does not form binary compounds with most of the 3*d* metals,[1–4] warranting the application of high-pressure synthesis to stabilize such compounds. Nevertheless, numerous theoretically predicted binary

and ternary compounds are included in the Quantum Materials Database (NaZnBi, Na_2ZnBi, $NaZn_2Bi$, $NaZnBi_2$),[10] Materials Project (ZnBi, $ZnBi_3$, $NaBi_3$, Na_3Zn, $NaZn_3$),[11] and AFLOW library ($NaZn_2Bi$, $NaZn_4Bi$, Na_2ZnBi),[12] making the investigation of the Na–Zn–Bi system promising.

In addition to the online open resources,[10–12] we have theoretically explored the Na–Zn–Bi system with our "in-house developed" AGA algorithm to obtain accurate guidance for follow-up experimental synthesis.[36–40] The AGA search consists of a conventional genetic algorithm (GA) and adaptive processes. In a conventional GA process, the auxiliary classical potential is used to optimize trial structures in a search pool. In an adaptive process, we renew the auxiliary potential by matching it to the density-functional theory (DFT) results on a small subset of the optimized structures in the pool. This strategy makes it possible to explore broad regions of configuration space very efficiently by keeping the accuracy of structure prediction. At every AGA step, trial structures are "altered" in the spirit of Darwin's theory of evolution. Structures with lower energies are reserved for the next step, whereas structures with higher energies are substituted by new ones that are generated from low-energy parent structures. After dozens of AGA iterations, a search pool gets populated densely by low-energy off-spring structures. In this way, the AGA can discover novel stable and metastable structures in a very broad configuration space, but, more importantly, the structures generated by AGA have low formation energies relative to elements. Therefore, the predicted compounds are relatively more stable and have higher chances to exist experimentally, whereas the structures in other online databases are widely distributed in terms of the magnitude of formation energy.[1–3]

A list of theoretically predicted compounds from an AGA search is compiled in Table S8, and the calculated convex hull of the Na–Zn–Bi system is presented in Figure 1. The first two candidates, $Na_{11}Zn_2Bi_5$ and NaZnBi, have the lowest formation energies (nearly 0 eV/atom) and are shown in red triangles. Compounds Na_6ZnBi_5, Na_4ZnBi_2, Na_4ZnBi, and $NaZn_2Bi_2$ have formation energies slightly above the convex-hull ($E_d \sim 0.02$–0.03 eV/atom, shown as orange triangles) and are likely to occur. A recent comparison between computational and experimental structures suggests that predicted structures with formation energies up to ~0.3 eV/atom should be experimentally accessible.[79] Other predicted phases are less stable ($E_d \sim 0.04$–0.15 eV/atom, green/blue triangles), including hypothetical compounds $Na_4Zn_9Bi_9$, $NaZn_3Bi_3$, $NaZn_4Bi_3$ compounds, isostructural to the experimentally reported compounds from the Na-Zn-Sb system.[34,35] Only $Na_{11}Zn_2Bi_5$ ($P\bar{1}$) and NaZnBi ($P4/nmm$) were experimentally observed (see below). Interestingly, AGA suggests a hexagonal-type structure (LiGaGe, $P6_3/mc$, $V/Z = 153.5$ Å^3) for NaZnBi, with a formation energy lower by 0.009 eV/atom compared to the experimentally determined tetragonal structure ($V/Z = 162.3$ Å^3) (Table S8). The hexagonal structure is typical for lithium zinc antimonides and bismuthides (Table 1),[1] where Li is surrounded by prisms of Zn and *Pn* atoms. There is a clear pattern for the structures of equiatomic *A*Zn*Pn* (Figure 2). As the atomic size of *A* or *Pn* increases, alkali

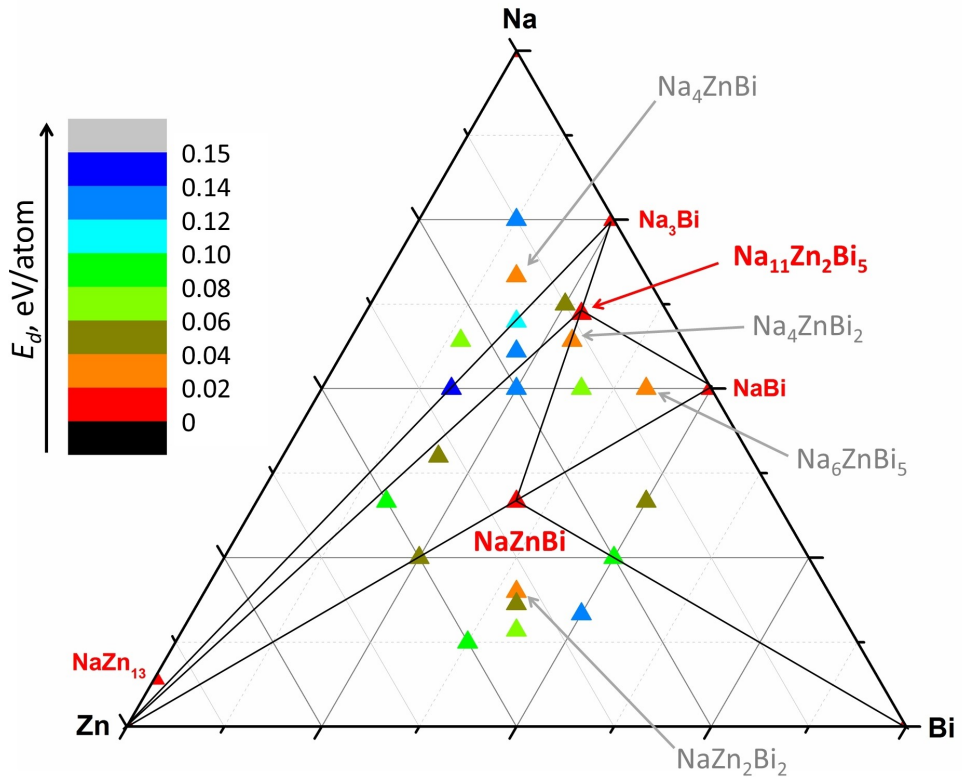

Figure 1. Convex-hull section of the Na–Zn–Bi system.

Table 1. Structure types among the equiatomic alkali metal zinc pnictides *AZnPn*

AZnPn	P	As	Sb	Bi
Li	MgAgAs[1]	MgAgAs[1]	LiGaGe,[1] MgAgAs[80]	LiGaGe[1]
Na	PbClF[1]	PbClF[1]	PbClF[1]	PbClF, this work
K	BeZrSi[1]	BeZrSi[1]	BeZrSi[1]	–
Rb	–	–	BeZrSi[49]	–
Cs	–	–	BeZrSi[49]	–

elements tend to have larger coordination polyhedral ranging from tetrahedra (MgAgAs type) to trigonal pyramids (PbClF type) to large hexagonal prisms (BeZrSi type) for the *AZnPn* phosphides and arsenides. For the antimonides, alkali metal coordination environment changes from tetrahedral (LiGaGe type) to square pyramidal (PbClF type) and finally to hexagonal prismatic (BeZrSi type). The same trend in alkali metal coordination polyhedron change with the size of *A* is observed for bismuthides, however *AZnBi* are represented by only two structure type: LiZnBi (LiGaGe type) and NaZnBi (PbClF type). Interestingly, two polymorphs are reported for LiZnSb: hexagonal LiGaGe ($P6_3/mc$) and cubic MgAgAs ($F\bar{4}3m$).[80] The cubic phase can only be prepared by a low-temperature solution-phase method,[80] otherwise, the hexagonal structure type is preferred. Therefore, it is possible that the hexagonal-type structure (LiGaGe, $P6_3/mc$) for NaZnBi predicted by AGA can be stabilized using a different synthetic approach.

Verification: hydride route screening and single-crystal diffraction

As the list of feasible compounds was established, a compositional space of the Na–Zn–Bi system was experimentally screened by the hydride route. A short heat treatment (723 K/13 h total) allowed for reliable verification in less than 24 h. As a result of phase analysis, NaZnBi (PbClF, *P4/nmm*) and $Na_{11}Zn_2Bi_5$ ($Na_{11}Cd_2Sb_5$, $P\bar{1}$) were confirmed from PXRD data, while other theoretically predicted compounds were not observed.

$NaZn_{1-x}Bi$ and $NaZn_{1-y}Bi$ phases. Interestingly, during the optimization of synthetic conditions for the preparation of NaZnBi, a more complex situation was uncovered. As seen in Figure 3, the sample with initial composition NaH:Zn:Bi = 1.05:1:1 yields ternary NaZnBi as the main phase with traces of unreacted elemental Bi and Zn. The slight excess of NaH as compared to stoichiometric amount is attributed to the 95% purity of commercially available NaH reactant. Surprisingly, with increasing the NaH content, the reaction is not completed, but, results in a secondary phase, as evidenced from the PXRD data. The content of this secondary phase approaches its maximum in the NaH:Zn:Bi = 1.5:1:1 loaded sample.

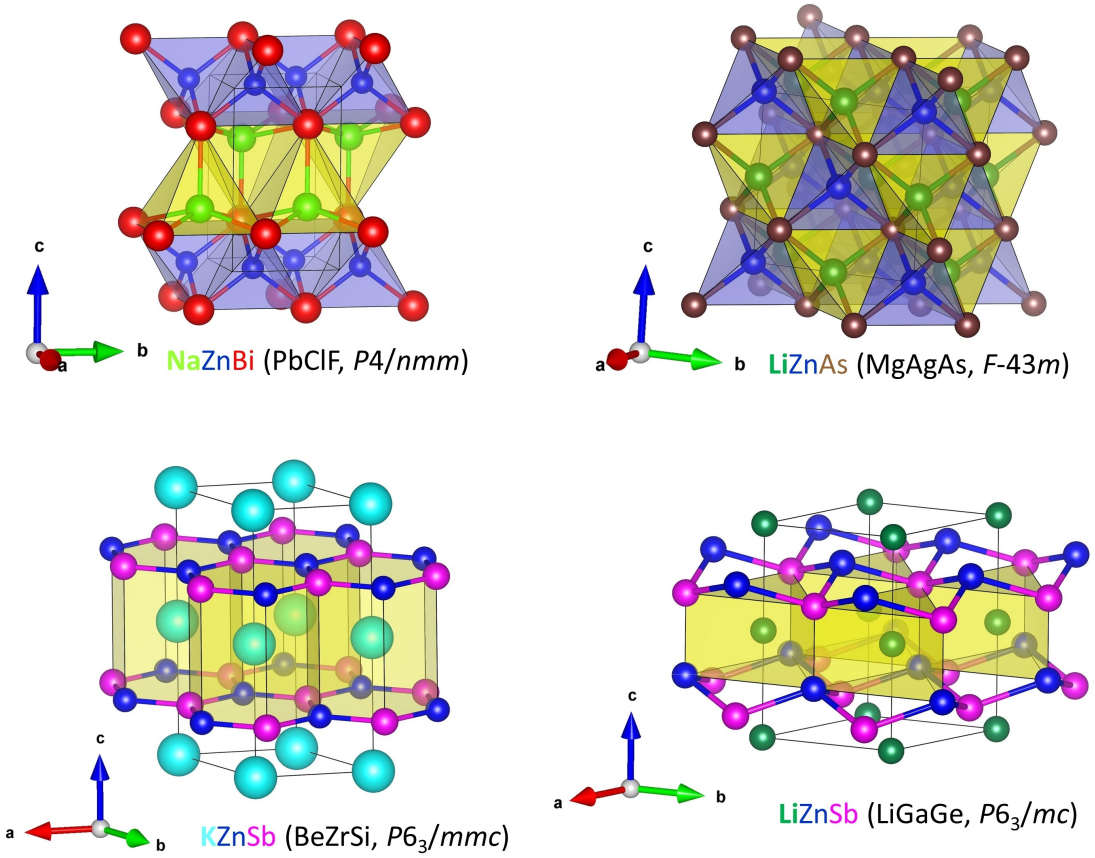

Figure 2. Structure types among the equiatomic alkali metal zinc pnictides *AZnPn*.

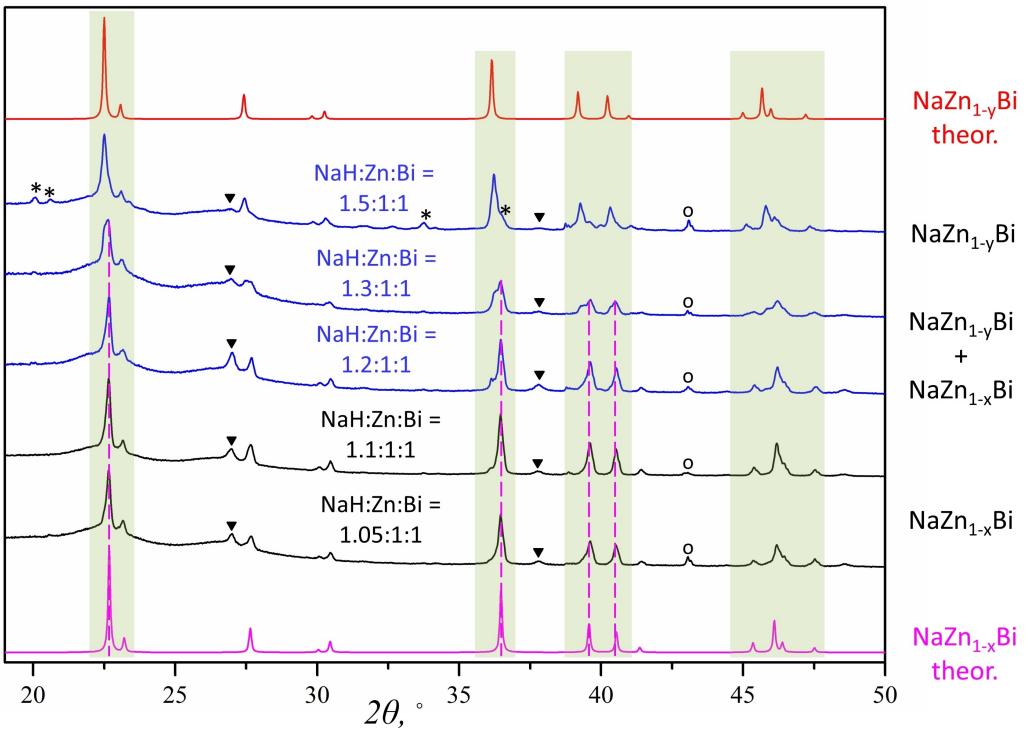

Figure 3. Evolution of PXRD patterns with increasing the NaH content. Above the 1.1:1:1 loading molar NaH:Zn:Bi ratio, the $NaZn_{1-y}Bi$ phase appears and reaches its maximum content in the sample with NaH:Zn:Bi loading ratio of 1.5:1:1. Minor impurities are marked as Bi(▼), Zn(o), $Na_{11-z}Zn_2Bi_5$ (*), respectively. Theoretical powder patterns of $NaZn_{1-x}Bi$ (bottom) and $NaZn_{1-y}Bi$ (top), simulated based on the single-crystal data, are provided for reference.

Analysis of the single crystal X-ray diffraction data (Table S1–S3) for the crystals selected from the slow-cooled samples with Na:Zn:Bi loading molar ratios of 1:1:1 and 1.5:1:1 indicates the same structure type (PbClF, *P4/nmm*). However, the structures differ in unit cell volumes and the occupancy factor for the Zn 2*a* site (Table 2). For the 1:1:1 loaded molar ratio, the $NaZn_{1-x}Bi$ phase with low Zn deficiency (x = 0.048(5)) is obtained. However, for higher alkali metal content (1.5:1:1 loading Na:Zn:Bi molar ratio) the $NaZn_{1-y}Bi$ phase with more Zn vacancies (y = 0.063(5)) is preferred. Regrinding and reheating of the samples with NaH:Zn:Bi = 1.3:1:1 molar ratio or longer annealing (60 h) still resulted in the coexistence of $NaZn_{1-x}Bi$ and $NaZn_{1-y}Bi$ (Figure S3). Variation of the Zn:Bi ratio, as in samples with NaH:Zn:Bi molar ratio of 1:1:1, 1:0.95:1, 1:0.9:1, 1:0.85:1, only leads to $NaZn_{1-x}Bi$ compound and an increased amount of Bi impurity (Figure S4), indicating that Na vapor pressure/concentration is crucial for stabilizing $NaZn_{1-y}Bi$. Combustion analysis, performed on the $NaZn_{1-y}Bi$ phase does not indicate significant content of H (< 0.03 wt.%).

Interestingly, with increasing vacancies at the Zn 2*a* sites, the unit cell parameters increase (Table 2, Figure 4). Therefore, characteristic Bragg peaks in the PXRD pattern of the $NaZn_{1-y}Bi$ phase are shifted to lower 2θ values (Figure 3). Increasing the size of the unit cell originates from the increased interatomic distances ($d_{Zn\text{-}Bi}$) inside the $ZnBi_4$ tetrahedra from 2.843(3) Å to 2.860(2) Å, while distances between the tetrahedra and alkali metal layers (i.e. $d_{2\,Na\text{-}Bi}$ = 3.266(1)–3.264(2) Å) remain the same (Table 2, Figure 4). The Bi–Bi distances in $ZnBi_4$ tetrahedra are long (~4.5–4.7 Å), indicating that there are no bonding interactions between Bi atoms. Thus, vacancies at Zn sites generate empty and expanded Bi_4 tetrahedra.

$Na_{11-z}Zn_2Bi_5$ phase. $Na_{11}Zn_2Bi_5$ ($Na_{11}Cd_2Sb_5$ structure type, $P\bar{1}$) was confirmed during screening of the Na–Zn–Bi system. A

Table 2. Crystallographic parameters and bond distances in the $NaZn_{1-x}Bi$ and $NaZn_{1-y}Bi$ phases (single crystal data at 100 K).

Refined composition	*a*, Å	*c*, Å	$d_{Zn\text{-}Bi}$, Å	$d_{1\,Na\text{-}Bi}$, Å	$d_{2\,Na\text{-}Bi}$, Å
$NaZn_{1-x}Bi$, x = 0.042(5)	4.5133(3)	7.5861(6)	2.8444(3)	3.305(1)	3.266(4)
$NaZn_{1-x}Bi$, x = 0.051(5)	4.5063(4)	7.5772(7)	2.8403(3)	3.299(1)	3.265(4)
$NaZn_{1-x}Bi$, x = 0.052(6)	4.5139(4)	7.5932(7)	2.8454(3)	3.306(1)	3.267(5)
average: x = 0.048(5)	4.511(4)	7.586(8)	2.843(3)	3.303(4)	3.266(1)
$NaZn_{1-y}Bi$, y = 0.058(6)	4.5387(3)	7.6176(7)	2.8600(3)	3.326(1)	3.264(5)
$NaZn_{1-y}Bi$, y = 0.062(5)	4.5375(3)	7.6066(5)	2.8578(3)	3.324(1)	3.263(4)
$NaZn_{1-y}Bi$, y = 0.069(5)	4.5428(3)	7.6184(6)	2.8614(3)	3.329(1)	3.266(4)
average: y = 0.063(5)	4.540(3)	7.614(7)	2.860(2)	3.326(3)	3.264(2)

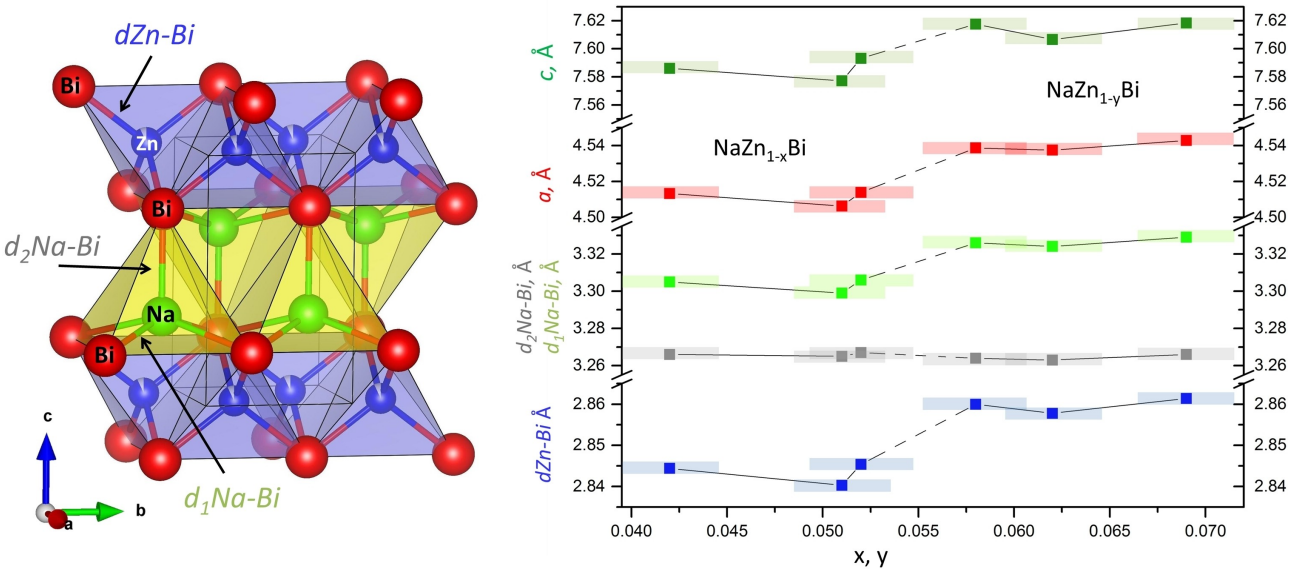

Figure 4. Variation of the unit cell parameters and bond distances in the $NaZn_{1-x}Bi$ and $NaZn_{1-y}Bi$ phases. Rectangles represent standard deviations of x and y. Standard deviations of the unit cell parameters and bond distances are ~100 times and ~10 times smaller than their corresponding symbols used. The abrupt change in *a*, *c*, $d_{Zn\text{-}Bi}$, $d_{1\ Na\text{-}Bi}$ is observed upon the transition from $NaZn_{1-x}Bi$ to $NaZn_{1-y}Bi$ phase. The interlayer distance ($d_{2\ Na\text{-}Bi}$) remains nearly the same.

lower temperature (573 K vs. 723 K), longer annealing time (48 h vs. 8 h), and excess of both NaH and Zn (loaded molar ratio NaH:Zn:Bi = 12.2:2.4:5) were necessary to prepare a phase pure sample (Figure S4). Single crystal X-ray diffraction analysis confirmed the $Na_{11}Cd_2Sb_5$ structure type (*P*-1),[1] although with some degree of disorder (Table S5). The crystal structure of the compound (Figure 5a) consists of columns with $[Zn_2Bi_5]^{11-}$ "butterfly" units surrounded by Na^+ cations. Compared to the ideal structure ($Na_{11}Cd_2Sb_5$ structure type), there is a minor disorder within the "butterfly" $[Zn_2Bi_5]^{11-}$ clusters, which are split along the *b*-direction with ~97% probability of the $[Zn(1)Zn(2)Bi_5]^{11-}$ cluster and 3% probability of the $[Zn(3)Zn(4)Bi_5]^{11-}$ cluster (Figure 5b). As a result, Na(2) atoms are absent in ~3% of cases, so the unrealistically short Na(2)-Zn(3) and Na(2)-Zn(4) interatomic distances of ~1.8–1.9 Å are avoided (Fig-

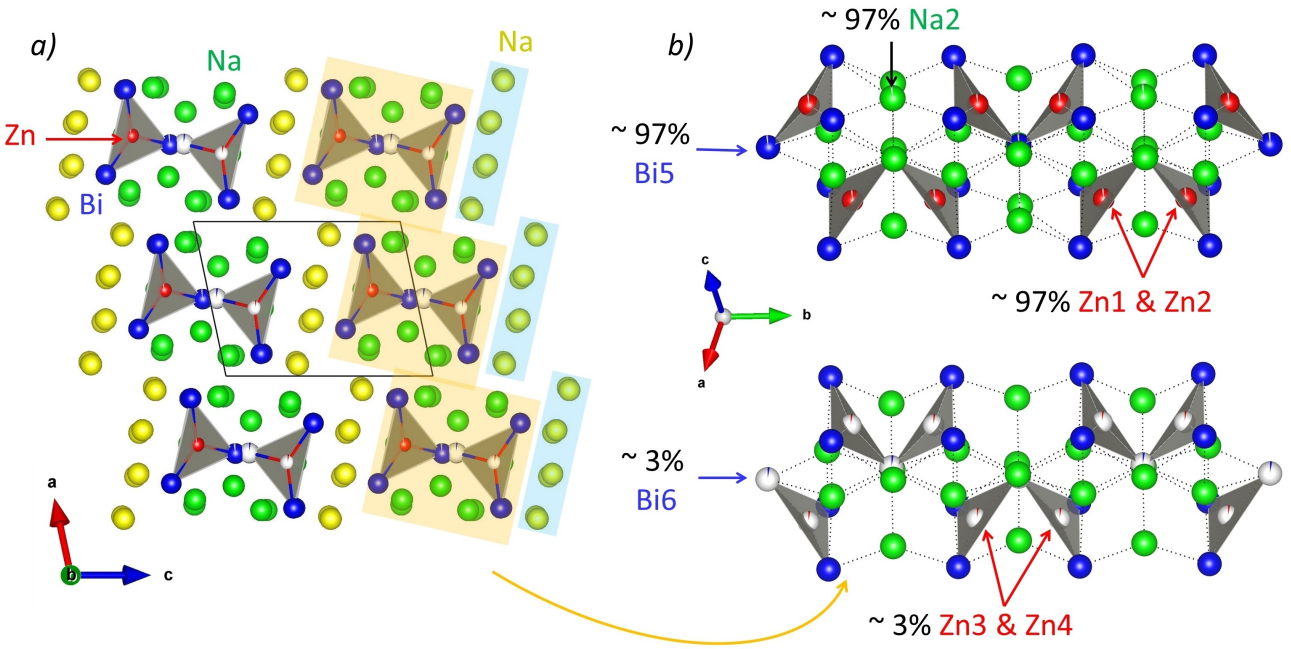

Figure 5. Crystal structure of the $Na_{11-z}Zn_2Bi_5$ compound: *a)* a projection in the *ac* plane; *b)* $[Zn_2Bi_5]^{11-}$ clusters considering the 97%/3% split model of the structure.

ure 5b), resulting in the composition $Na_{11-z}Zn_2Bi_5$, $z = 0.0297(5)$, as refined from single crystal X-ray diffraction data at 100 K.

Band structures and bonding

Band structures, as well as total and partial density of states (DOS) (Figure 6) for stoichiometric NaZnBi and $Na_{11}Zn_2Bi_5$ were calculated using the Vienna ab initio simulation package (VASP). For these compounds, Bi and Zn atomic wavefunctions have major contributions to the occupied states. This is in accordance with each Na atom formally donating its valence electron to the [Zn–Bi] covalent framework. NaZnBi is predicted to be metallic with a non-zero density of states at the Fermi level, whereas $Na_{11}Zn_2Bi_5$ is semimetallic with a very narrow band gap ~0.035 eV. As demonstrated by the partial DOS curves for NaZnBi (Figure 6, right), the narrow peak around 5 eV below the Fermi level is dominated by Zn 4*s* and Bi 6*p* orbitals, and the broader bands ranging from 3.5 eV below the Fermi level are mostly composed of Bi 6*p* orbitals with minor contributions from Zn 3*d*, 4*p* and Na 3*s* valence orbitals.

The partially vacant 2*a* sites in the structures of $NaZn_{1-x}Bi$ and $NaZn_{1-y}Bi$ can be rationalized from analysis of the crystal orbital Hamilton population (COHP) diagrams of the idealized "NaZnBi" structure. The COHP curves obtained from the VASP output using LOBSTER code (Figure 7b)[64,65] reveals the onset of a pseudogap in the DOS occurring at a Fermi level corresponding to stoichiometric "NaZnBi" (18.0 valence electrons) and optimized Zn–Bi interactions. Below this Fermi level, there are Zn–Zn antibonding states, with optimized Zn–Zn pairwise interactions occurring for "$NaZn_{0.89}Bi$" (16.7 valence electrons) or $x = 0.11$ in $NaZn_{1-x}Bi$. Although this analysis rationalizes the occurrence of vacancies at the Zn sites, the predicted vacancy concentration by VASP is larger than the observed values.

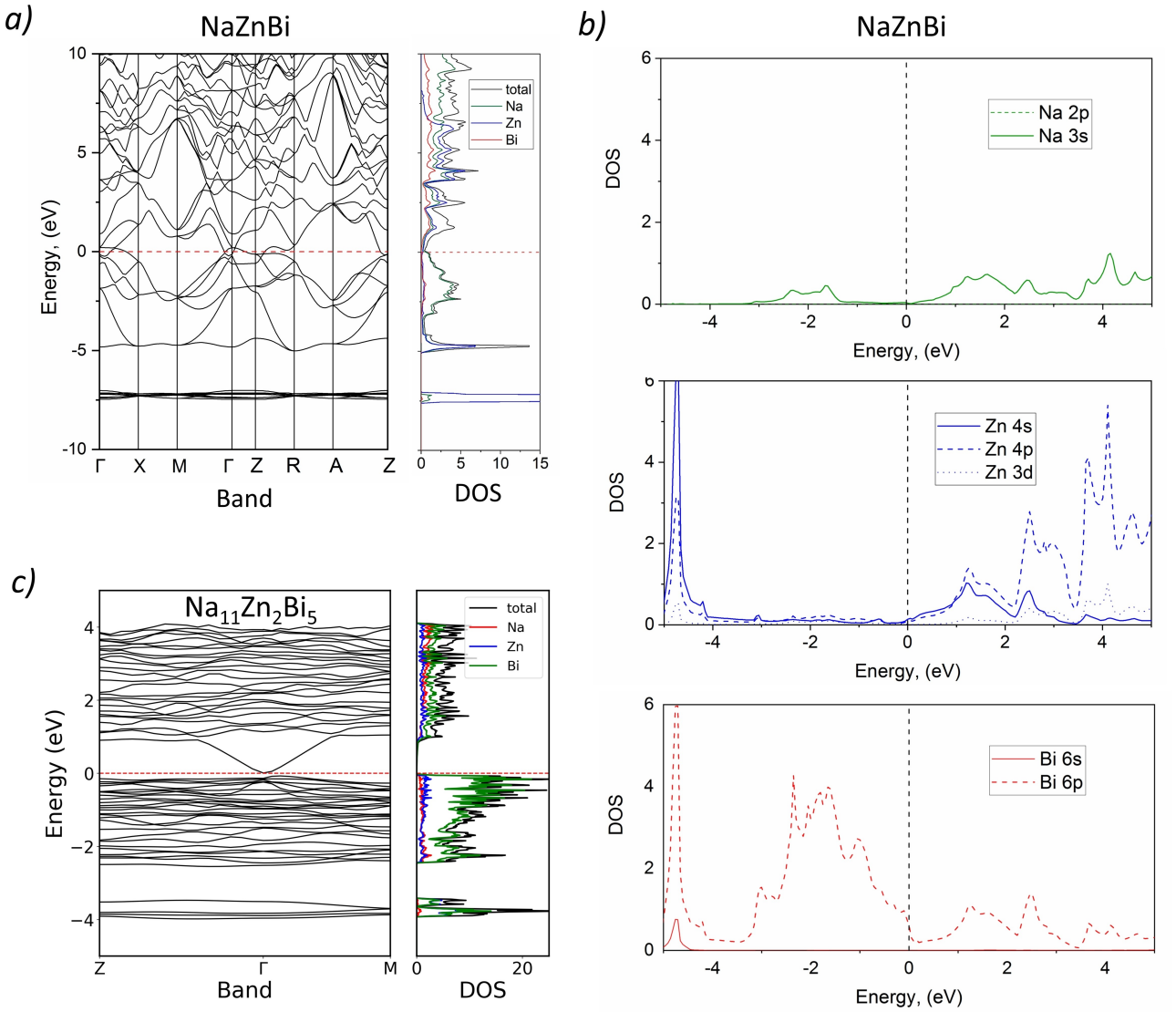

Figure 6. Band structures with total and partial DOS representations for *a)* NaZnBi and *c)* $Na_{11}Zn_2Bi_5$ compounds. The zero energy is taken at the Fermi level E_F. The contribution of selected orbitals from Na, Zn and Bi atoms into DOS of NaZnBi is shown on the right *b)*.

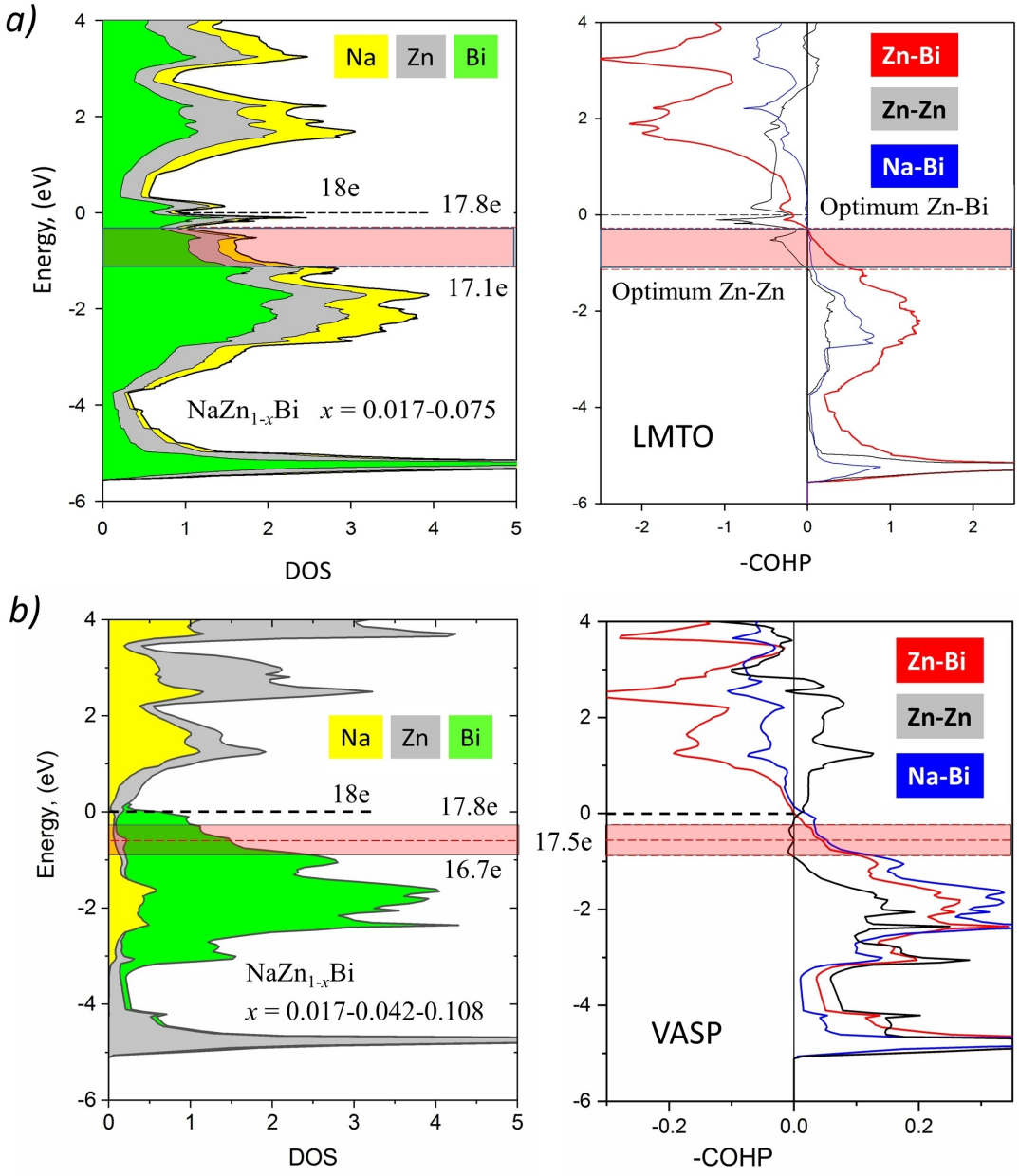

Figure 7. COHP diagram of the electronic structure of ideal NaZnBi compound calculated using *a)* LMTO and *b)* VASP-LOBSTER. Optimized Zn–Zn and Zn–Bi interactions are realized by introducing Zn vacancies (x = 0.017–0.108).

Therefore, we examined the electronic structure and similar COHP curves using the LMTO approach (Figure 7 a). The results are qualitatively similar to the VASP outcome, although the features of the DOS and COHP curves close to the Fermi level for stoichiometric "NaZnBi" differ between the two methods. The onset of the pseudogap in the LMTO DOS curve occurs above 18.0 valence electrons. Likewise, the COHP curves suggest "$NaZn_{0.98}Bi$" (17.8 valence electrons; $x = 0.017$) optimizes Zn–Bi orbital interactions and "$NaZn_{0.93}Bi$" (17.1 valence electrons; $x = 0.075$) optimizes Zn–Zn orbital interactions. Regardless of the specific differences between VASP and LMTO, a consistent rationale for the occurrence of Zn vacancies is to alleviate Zn–Zn antibonding interactions.

Similar examples of defect structures are also found among pnictides of rare-earth metal and Ni or Cu: $RNi_{2-x}Sb_2$ (R = La, Ce, Pr, Nd, Sm, Gd, Tb, Dy, Ho, Er) and $RNi_{2-x}Bi_2$ (R = La, Ce, Pr, Nd, Sm, Gd, Tb, Dy) phases with the $CaBe_2Ge_2$ (*P4/mmm*) structure type, and $SrNi_{2-x}Sb_2$, $EuNi_{2-x}Sb_2$, $SrCu_{2-x}P_2$ and $CaCu_{2-x}P_2$ with the $ThCr_2Si_2$ (*I4/mmm*) structure type.[81–84] The crystal structures of these compounds contain Ni(Cu)Pn_4 tetrahedra and are related to the PbClF type (*P4/nmm*) of $NaZn_{1-x}Bi$ and $NaZn_{1-y}Bi$. It was also proposed that vacancies on the Ni or Cu sites might stabilize the structure because additional valence electrons provided by the missing atoms would occupy antibonding states.[81–84]

In situ synchrotron X-ray diffraction

In situ synchrotron powder X-ray diffraction data of samples with the loading NaH:Zn:Bi compositions of 1:1:1 (containing $NaZn_{1-x}Bi$ as the main phase) and 2:1:1 (containing mainly $NaZn_{1-y}Bi$ and $Na_{11-z}Zn_2Bi_5$) are shown in Figure 8. Above 519 K, only $NaZn_{1-x}Bi$ with traces of ZnO is present while Bi (as the main impurity) is molten. With further increase in the temperature above 789 K, $NaZn_{1-x}Bi$ phase melts and recrystallizes later on cooling below 791 K. However, the corresponding XRD powder pattern (Figure S5) indicates considerable preferred orientation arising from the formation of comparably large single crystals of $NaZn_{1-x}Bi$ upon cooling in the presence of a molten Bi acting as flux.

$NaZn_{1-y}Bi$ melts at 785 K, at around the same temperature as $NaZn_{1-x}Bi$, and recrystallizes on cooling below 778 K. $Na_{11-z}Zn_2Bi_5$ is significantly less thermally stable. Above 611 K it decomposes to $NaZn_{1-y}Bi$ and another unknown phase (Figures 8b, 9, 10), later determined to be high-temperature polymorph *HT*-Na_3Bi (BiF_3, *Fm*-3*m*) (Table S8, Figure S2). Interestingly, this structure type was earlier reported for the high-pressure polymorph *HP*-Na_3Bi above 0.5 GPa.[57] *HT*-Na_3Bi cannot be stabilized at room temperature by quenching, but *RT*-Na_3Bi (Na_3As, $P6_3/mmc$)[85] forms instead. As can be seen from Table 3, this hexagonal-type

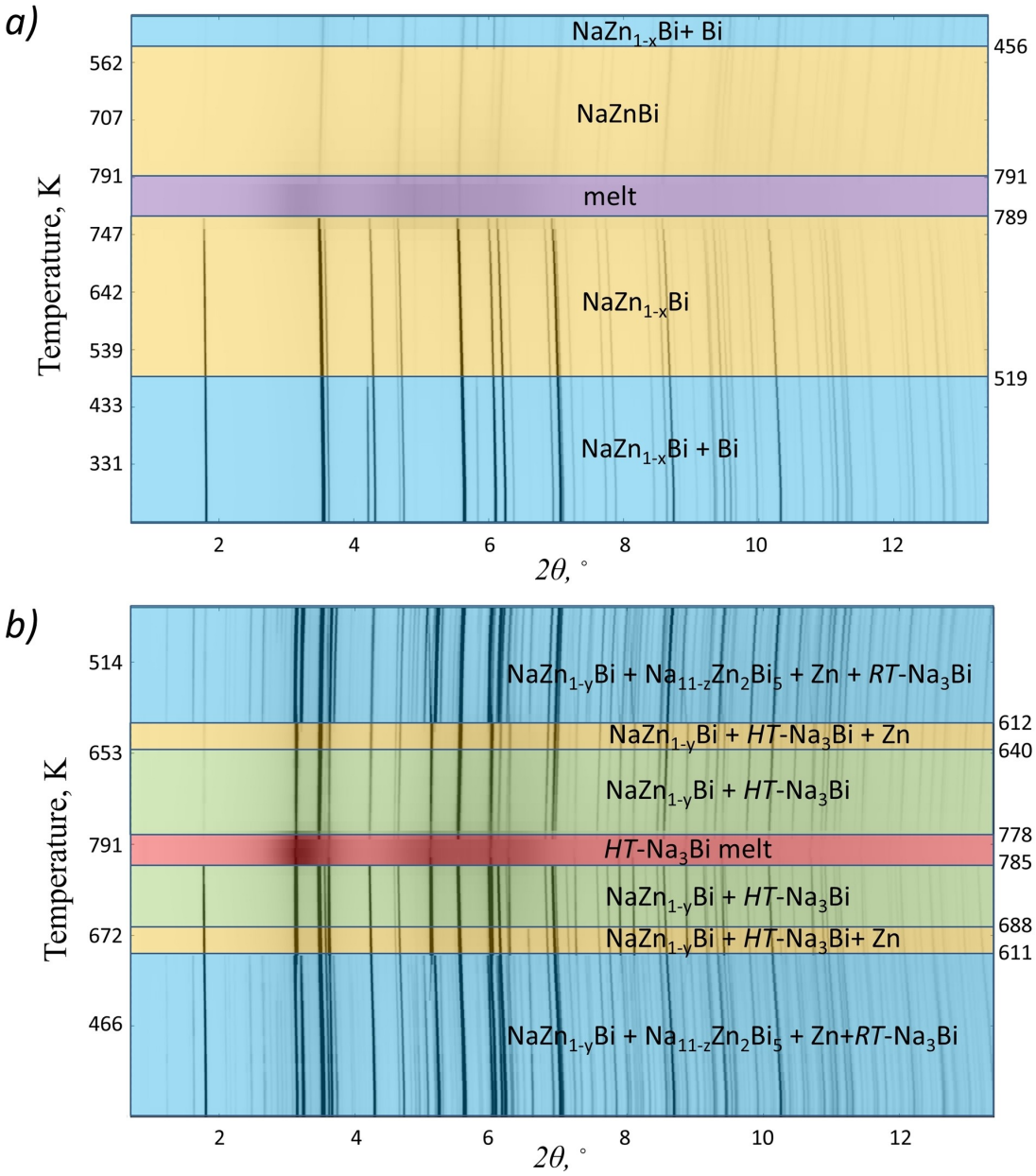

Figure 8. High-temperature in situ X-ray powder diffraction patterns showing transformations of powdered samples with initial NaH:Zn:Bi loading compositions of *a)* 1:1:1 (sample contains $NaZn_{1-x}Bi$ as main phase) and *b)* 2:1:1 (sample contains mainly $NaZn_{1-y}Bi$ and $Na_{11-z}Zn_2Bi_5$). The "waterfall" plot shows pattern evolution with the temperature change 298 K→820 K→298 K. The temperature regions with distinct phase contributions are highlighted in different colors.

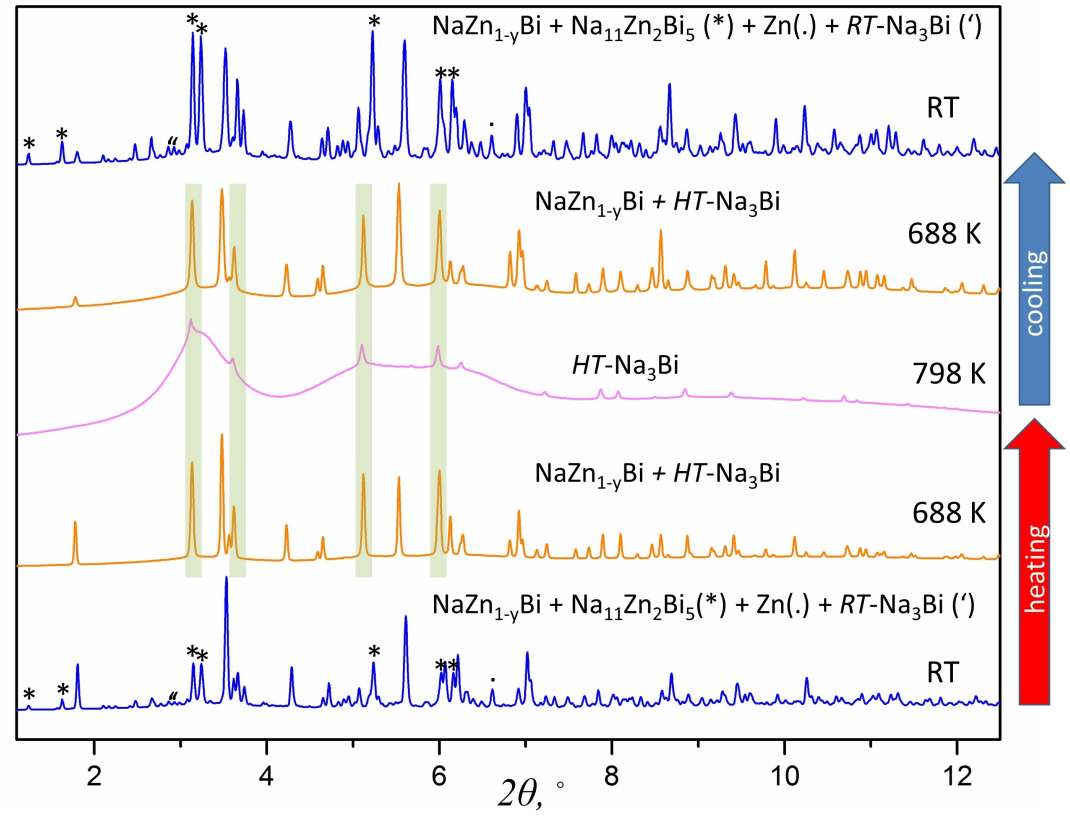

Figure 9. Selected X-ray powder diffraction patterns collected at RT, 688 K, 798 K on heating and cooling of the sample with loading NaH : Zn : Bi composition = 2 : 1 : 1; sample contains mainly $NaZn_{1-y}Bi$ and $Na_{11-z}Zn_2Bi_5$. The diffraction peaks attributed to *HT*-Na_3Bi are highlighted in green.

Table 3. Structure types among the alkali metal manganese pnictides Na_3Pn.

Compound	Structure type/condition
Na_3P	Na_3As ($P6_3/mmc$), RT[85]
Na_3As	Cu_3P ($P6_3/cm$), RT[86]
	BiF_3 (Fm-3m), HP[87]
Na_3Sb	Na_3As ($P6_3/mmc$), RT[85]
	BiF_3 (Fm-3m), HP[57]
Na_3Bi	Na_3As ($P6_3/mmc$), RT[85]
	BiF_3 (Fm-3m), HP[57]
	BiF_3 (Fm-3m), HT, this work

structure is common for all Na_3Pn compounds. The structure of Na_3As initially reported was re-determined to be a more complicated Cu_3P ($P6_3/cm$) type.[85,86] In the cases Pn = As, Sb, or Bi, high-pressure cubic BiF_3 type ($Fm\bar{3}m$) polymorphs were reported.[57,87] We calculated the thermodynamic properties of Na_3Bi with cubic (BiF_3) and hexagonal-type (Na_3As) from phonon frequencies within the harmonic approximation (QHA). It can be seen from Figure 10 that the Gibbs free energy of the cubic structure is indeed lower than that of the hexagonal structure when temperature exceeds ~122 K, and this trend is more pronounced at elevated temperatures. Band structure calculations of binary sodium bismuthides were reported earlier,[88] including hexagonal Na_3Bi and the high-pressure cubic polymorph, and both are predicted to be 3D topological Dirac semimetals.

Unit cell parameters, obtained from Rietveld refinements of the in situ synchrotron PXRD data for $NaZn_{1-x}Bi$, $NaZn_{1-y}Bi$, $Na_{11-z}Zn_2Bi_5$ and *HP*-Na_3Bi, increase almost linearly upon heating (Figure S5). The coefficients of thermal expansion (CTE (a) = $\frac{da}{dT}\times\frac{1}{a}$, CTE ($c$) = $\frac{dc}{dT}\times\frac{1}{c}$ =, CTE (V) = $\frac{dV}{dT}\times\frac{1}{V}$) obtained from linear fits of the data are in the range ~10^{-5}–10^{-4} K^{-1}. Taking into account the thermal stabilities of the $NaZn_{1-x}Bi$ (mp ~ 789 K), $NaZn_{1-y}Bi$ (mp ~ 785 K), and $Na_{11-z}Zn_2Bi_5$ (mp ~ 611 K), appropriate annealing temperatures were selected for their syntheses (723 K, 723 K and 573 K, respectively).

Conclusions

A combination of theoretical calculations, rapid compositional screening, and in situ diffraction study have resulted in discovery of 4 new phases in the previously "empty" Na–Zn–Bi system. On the one hand, theoretical computations by the AGA method correctly assessed the convex-hull of the Na–Zn–Bi system, and the predicted compounds with low formation energies were confirmed. On the other hand, experimental studies have shown that the list of predicted compounds cannot be solely accepted based on theory, but rather can serve as a guide for the experimentalist. For instance, the AGA

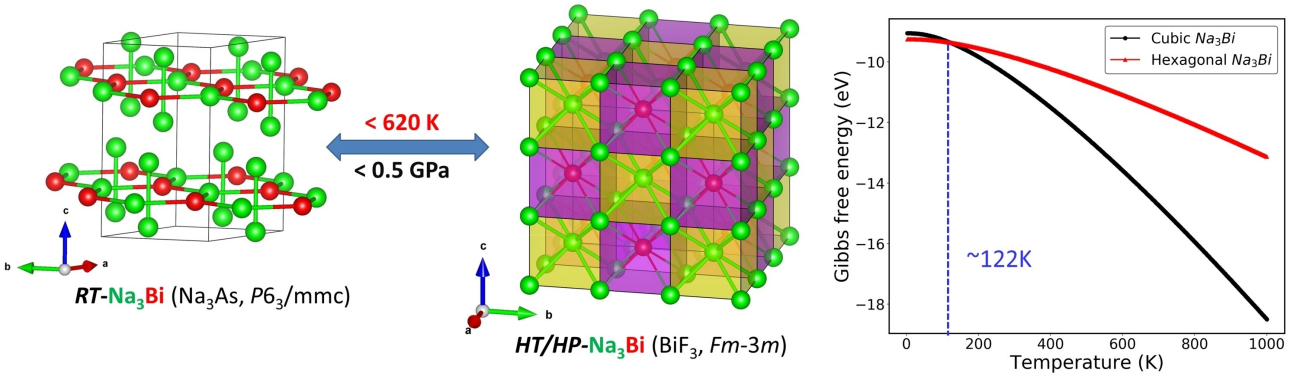

Figure 10. Crystal structures of Na_3Bi polymorphs (left) and their calculated Gibbs free energies (right), showing higher stability of the cubic structure above ~122 K.

suggests that the hexagonal LiGaGe-type structure ($P6_3/mc$) has a 0.009 eV/atom lower formation energy compared to the tetragonal PbClF-type ($P4/nmm$), although the tetragonal structure was confirmed experimentally for "NaZnBi". Moreover, the ideal "NaZnBi" stoichiometry is not observed, but two defect phases $NaZn_{1-x}Bi$ ($x = 0.048(5)$, $V = 154.4(4)$ Å^3) and $NaZn_{1-y}Bi$ ($y = 0.063(5)$, $V = 156.9(4)$ Å) were found in close proximity to the stoichiometric 1:1:1 ratio. Vacancies on the Zn sites can be rationalized from the optimized Zn–Zn and Zn–Bi bonding interactions as evidenced from electronic structure calculations. *In situ* powder X-ray diffraction should be an integral part of a search for new structures because it can shed light on the existence of metastable or stable in a narrow temperature range phases. Specifically, by means of such in situ experiments, a high-temperature *HT*-Na_3Bi (BiF_3, Fm-3m) polymorph was discovered, which is isostructural to high-pressure polymorph *HP*-Na_3Bi.

Note added in proof: After acceptance of this manuscript we became aware of the work of Shilov et al.,[89] reporting crystal structure of the NaZnBi compound grown from Bi-flux. Their study confirms NaZnBi structure determined here, albeit without Zn deficiency.

Associated content

Rietveld refinement plots, Powder patterns, tables with parameters of XRD data collection and refinement can be found in the Supporting Information.

Acknowledgements

We thank Dr. Wenqian Xu and Dr. Andrey Yakovenko at 17-BM beamline, APS ANL, for help with high-temperature synchrotron powder XRD data collection. Financial support from the National Science Foundation (DMR-1944551) CAREER award is gratefully acknowledged. The work at Ames Laboratory was supported by the U.S. Department of Energy (DOE), Office of Science, Basic Energy Sciences, Materials Science and Engineering Division, under Contract No. DE-AC02-07CH11358, including a grant of computer time at the National Energy Research Scientific Computing Center (NERSC) in Berkeley, CA. Use of the Advanced Photon Source at Argonne National Laboratory was supported by the U. S. Department of Energy, Office of Science, Office of Basic Energy Sciences, under Contract No. DE-AC02-06CH11357. The work at the University of Science and Technology of China was supported by the National Natural Science Foundation of China (11774324 & 12074362) and the computing time at the Supercomputing Center of University of Science and Technology of China. The work at Guangdong University of Technology was supported by the Guangdong Natural Science Foundation of China (Grant No. 2017B030306003, and No. 2019B1515120078).

Conflict of Interest

The authors declare no conflict of interest.

Keywords: alkali metals · crystal structure prediction algorithm · hydrides · solid-state structures · X-ray diffraction

[1] G. Bergerhoff, I. D. Brown, in „Crystallographic Databases", F. H. Allen, G. Bergerhoff, R. Sievers (Hrsg.) Chester, International Union of Crystallography, **1987**.
[2] C. R. Groom, I. J. Bruno, M. P. Lightfoot, S. C. Ward, *Acta Crystallogr.* **2016**, *B72*, 171–179.
[3] P. Villars, K. Cenzual, Pearson's Crystal Data: Crystal Structure Database for Inorganic Compounds (on DVD), Release 2019/20, ASM International®, Materials Park, Ohio, USA.
[4] See https://paulingfile.com/ for information about binary compounds.
[5] C. J. Pickard, R. Needs, *J. Phys. Condens. Matter* **2011**, *23*, 053201.
[6] J. Pannetier, J. Bassas-Alsina, J. Rodriguez-Carvajal, V. Caignaert, *Nature* **1990**, *346*, 343–345.
[7] A. R. Oganov, C. W. Glass, *J. Chem. Phys.* **2006**, *124*, 244704.
[8] Y. Wang, J. Lv, L. Zhu, Y Ma, *Phys. Rev. B: Condens. Matter Mater. Phys.* **2010**, *82*, 094116.
[9] Y. Wang, Lv, J. L. Zhu, Y Ma, *Comput. Phys. Commun.* **2012**, *183*, 2063–2070.
[10] J. E. Saal, S. Kirklin, M. Aykol, B. Meredig, C. Wolverton, *JOM* **2013**, *65*, 1501–1509.
[11] D. Richards, S. Dacek, S. Cholia, D. Gunter, D. Skinner, G. Ceder, *APL Mater.* **2013**, *1*, 011002.

[12] See https://cmr.fysik.dtu.dk/ for Computational Materials Repository.
[13] See http://gurka.fysik.uu.se/ESP/ for information about electronic structure of materials.
[14] S. Curtarolo, W. Setyawan, S. Wang, J. Xue, K. Yang, R. H. Taylor, L. J. Nelson, G. L. W. Hart, S. Sanvito, M. Buongiorno-Nardelli, *Comput. Mater. Sci.* **2012**, *58*, 227.
[15] M. de Jong, W. Chen, T. Angsten, A. Jain, R. Notestine, A. Gamst, M. Sluiter, C. K. Ande, S. van der Zwaag, J. J. Plata, *Sci. Data* **2013**, *2*, 150009.
[16] K. Alberi, M. B. Nardelli, A. Zakutayev, L. Mitas, S. Curtarolo, A. Jain, M. Fornari, N. Marzari, I. Takeuchi, M. L. Green, M. Kanatzidis, M. F. Toney, S. Butenko, B. Meredig, S. Lany, U. Kattner, A. Davydov, E. S. Toberer, V. Stevanovic, A. Walsh, N. G. Park, A. Aspuru-Guzik, D. P. Tabor, J. Nelson, J. Murphy, A. Setlur, J. Gregoire, H. Li, R. Xiao, A. Ludwig, L. W. Martin, A. M. Rappe, S. H. Wei, J. Perkins, *J. Phys. D* **2019**, *52*, 013001.
[17] S. Lotfi, Z. Zhang, G. Viswanathan, K. Fortenberry, A. M. Tehrani, J. Brgoch, *Matter.* **2020**, *3*, 261–272.
[18] S. Lotfi, J. Brgoch, *Chem. Eur. J.* **2020**, *26*, 8689–8697.
[19] A. O. Oliynyk, E. Antono, T. D. Sparks, L. Ghadbeigi, M. W. Gaultois, B. Meredig, A. Mar, *Chem. Mater.* **2016**, *28*, 7324–7331.
[20] A. O. Oliynyk, A. Mar, *Acc. Chem. Res.* **2018**, *51*, 59–68.
[21] R. Gautier, X. Zhang, L. Hu, L. Yu, Y. Lin, T. O. L. Sunde, D. Chon, K. R. Poeppelmeier, A. Zunger, *Nat. Chem.* **2015**, *7*, 308–316.
[22] J. Schmidt, W. Schnelle, Yu. Grin, R. Kniep, *Solid State Sci.* **2003**, *5*, 535–539.
[23] J. Schmidt, R. Niewa, M. Schmidt, Yu. Grin, *J. Am. Ceram. Soc.* **2005**, *88/7*, 1870–1874.
[24] N. Reinfried, J. Schmidt, B. Kieback, Yu. Grin, *Proceedings PM2004 Powder Metallurgy World Congress*, Wien, **2004**, p. 247.
[25] X. Ma, F. Xu, T. M. Atkins, A. M. Goforth, D. Neiner, A. Navrotsky, S. M. Kauzlarich, *Dalton Trans.* **2009**, *0*, 10250–10255.
[26] T. Yi, S. Chen, S. Li, H. Yang, S. Bux, Z. Bian, N. A. Katcho, A. Shakouri, N. Mingo, J. P. Fleurial, N. D. Browning, S. M. Kauzlarich, *J. Mater. Chem.* **2012**, *22*, 24805–24813.
[27] J. V. Zaikina, M. Batuk, A. M. Abakumov, A. Navrotsky, S. M. Kauzlarich, *J. Am. Chem. Soc.* **2014**, *136*, 16932–16939.
[28] J. V. Zaikina, M. Y. Kwong, B. Baccam, S. M. Kauzlarich, *Chem. Mater.* **2018**, *30*, 8883–8890.
[29] T. Cox, V. Gvozdetskyi, B. Owens-Baird, J. V. Zaikina, *Chem. Mater.* **2018**, *30*, 8707–8715.
[30] V. Gvozdetskyi, M. P. Hanrahan, R. A. Ribeiro, T. Kim, L. Zhou, A. J. Rossini, P. C. Canfield, J. V. Zaikina, *Chem. Eur. J.* **2019**, *25*, 4123–4135.
[31] V. Gvozdetskyi, G. Bhaskar, M. Batuk, X. Zhao, R. Wang, S. L. Carnahan, M. P. Hanrahan, R. A. Ribeiro, P. C. Canfield, A. J. Rossini, C. Z. Wang, K.-M. Ho, J. Hadermann, J. V. Zaikina, *Angew. Chem. Int. Ed.* **2019**, *58*, 15855–15862.
[32] C. J. Perez, V. J. Bates, S. M. Kauzlarich, *Inorg. Chem.* **2019**, *58*, 1442–1450.
[33] V. Gvozdetskyi, B. Owens-Baird, S. Hong, J. V. Zaikina, *Materials.* **2019**, *12*, 48–62.
[34] V. Gvozdetskyi, B. Owens-Baird, S. Hong, T. Cox, G. Bhaskar, C. Harmer, Y. Sun, F. Zhang, C. Zh, Wang, K. M. Ho, J. V. Zaikina, *Chem. Mater.* **2019**. *31*, 8695–8707.
[35] V. Gvozdetskyi, L. Shannon, B. Owens-Baird, J.-A. Dolyniuk, T. Cox, R. Wang, Z. Lin, K.-M. Ho, J. V. Zaikina, *Inorg. Chem.* **2021**, *60*, 10686–10697.
[36] M. Ji, K. Umemoto, C. Z. Wang, K. M. Ho, R. M. Wentzcovitch, *Phys. Rev. B* **2011**, *84*, 220105.
[37] S. Q. Wu, M. Ji, C. Z. Wang, M. C. Nguyen, X. Zhao, K. Umemoto, R. M. Wentzcovitch, K.-M. Ho, *J. Phys. Condens. Matter.* **2014**, *26*, 035402.
[38] X. Zhao, M. C. Nguyen, W. Y. Zhang, C. Z. Wang, M. J. Kramer, D. J. Sellmyer, X. Z. Li, F. Zhang, L. Q. Ke, V. P. Antropov, K.-M. Ho, *Phys. Rev. Lett.* **2014**, *112*, 045502.
[39] R. Wang, Y. Sun, V. Antropov, Z. Lin, C.-Z. Wang, K.-M. Ho, *Appl. Phys. Lett.* **2019**, *115*, 182601.
[40] R. Wang, Y. Sun, V. Gvozdetskyi, X. Zhao, F. Zhang, L.-H. Xu, J. V. Zaikina, Z. Lin, C.-Z. Wang, K.-M. Ho, *J. Appl. Phys.* **2020**, *127*, 094902.
[41] A. S. Haynes, C. C. Stoumpos, H. Chen, D. Chica, M. G. Kanatzidis, *J. Am. Chem. Soc.* **2017**, *139*, 10814–10821.
[42] D. P. Shoemaker, Y. J. Hu, D. Y. Chung, G. J. Halder, P. J. Chupas, L. Soderholm, J. F. Mitchell, M. G. Kanatzidis, *PNAS.* **2014**, *111*, 10922–10927.
[43] G. Vasquez, A. Huq, S. E. Latturner, *Inorg. Chem.* **2019**, *58*, 8111–8119.
[44] S. R. Brown, S. M. Kauzlarich, F. Gascoin, G. J. Snyder, *Chem. Mater.* **2006**, *18*, 1873–1877.
[45] Y. Hu, G. Cerretti, E. L. Kunz Will, S. K. Bux, S. M. Kauzlarich, *J. Solid State Chem.* **2019**, *271*, 88–102.
[46] E. S. Toberer, A. F. May, B. C. Melot, E. Flage-Larsend, G. J. Snyder, *Dalton Trans.* **2010**, *39*, 1046–1054.
[47] F. Gascoin, S. Ottensmann, D. Stark, S. M. Haile, G. J. Snyder, *Adv. Funct. Mater.* **2005**, *15*, 1860–1864.
[48] C. Chen, W. Xue, X. Li, Y. Lan, Z. Zhang, X. Wang, F. Zhang, H. Yao, S. Li, J. Sui, P. Han, X. Liu, F. Cao, Y. Wang, Q. Zhang, *Appl. Mater. Interf.* **2019**, *11*, 37741–37747.
[49] B. Owens-Baird, L.-L. Wang, S. Lee, K. Kovnir, *ZAAC* **2020**, *646*, 1079–1085.
[50] Q. D. Gibson, M. L. Schoop, L. Muechler, L. S. Xie, M. Hirschberger, N. P. Ong, R. Car, R. J. Cava, *Phys. Rev. B* **2015**, *91*, 205128.
[51] PDXL: Integrated X-ray powder diffraction software, Version 2.8.1.1. Rigaku, **2018**.
[52] Apex3, Version 2017.3, Bruker, USA.
[53] G. M. Sheldrick, *Acta Crystallogr.* **2008**, *A64*, 112–122.
[54] K. Momma, F. Izumi, *J. Appl. Crystallogr.* **2011**, *44*, 1272–1276.
[55] P. J. Chupas, K. W. Chapman, C. Kurtz, J. C. Hanson, P. L. Lee, C. P. Grey, *J. Appl. Crystallogr.* **2008**, *41*, 822–824.
[56] B. H. Toby, R. B. Von Dreele, *J. Appl. Crystallogr.* **2013**, *46*, 544–549.
[57] M. E. Leonova, I. K. Bdikin, S. A. Kulinich, O. K. Gulish, L. G. Sevast'yanova, K. P. Burdina, *Inorg. Mater.* **2003**, *39/3*, 266–270.
[58] G. Kresse, J. Furthmuller, *Comput. Mater. Sci.* **1996**, *6*, 15–50.
[59] G. Kresse, J. Furthmuller, *Phys. Rev. B* **1996**, *54*, 11169–11186.
[60] G. Kresse, D. Joubert, *Phys. Rev. B* **1999**, *59*, 1758–1775.
[61] P. E. Bloechl, *Phys. Rev. B* **1994**, *50*, 17953–17979.
[62] J. P. Perdew, K. Burke, M. Ernzerhof, *Phys. Rev. Lett.* **1996**, *77*, 3865–3868.
[63] H. J. Monkhorst, J. D. Pack, *Physical Rev. B* **1976**, *13*, 5188.
[64] R. Dronskowski, P. E. Blöchl, *J. Phys. Chem.* **1993**, *97*, 8617–8624.
[65] S. Maintz, V. L. Deringer, A. L. Tchougreeff, R. Dronskowski, *J. Comput. Chem.* **2016**, *37*, 1030–1035.
[66] O. K. Andersen, *Phys. Rev. B* **1975**, *12*, 3060–3083.
[67] O. K. Andersen, O. Jepsen, *Phys. Rev. Lett.* **1984**, *53*, 2571–2574.
[68] O. K. Andersen, O. Jepsen, D. Glötzel, W. R. L. Lambrecht, in *Highlights of CondensedMatter Theory* (Eds.: F. Bassani, F. Fumi and M. P. Tosi) NorthHolland, New York, **1985**.
[69] O. K. Andersen, *Phys. Rev. B* **1986**, *34*, 2439–2449.
[70] U. Barth, L. Hedin, *J. Phys. C* **1972**, *5*, 1629–1642.
[71] D. Koelling, B. N. Harmon, *J. Phys. C* **1977**, *10*, 3107–3114.
[72] O. Jepsen, O. K. Andersen, *Z. Phys. B* **1995**, *97*, 35–47.
[73] P. E. Blöchl, O. Jepsen, O. K. Andersen, *Phys. Rev. B* **1994**, *49*, 16223–16233.
[74] R. Pothin, R. M. Ayral, A. Berche, D. Granier, F. Rouessac, P. Jund, *Chem. Eng. J.* **2016**, *299*, 126–134.
[75] C. T. Lo, B. R. Ortiz, E. Toberer, A. He, V. Svitlyk, D. Chernyshov, T. Kolodiazhny, S. Lidin, Y. Mozharivskyj, *Chem. Mater.* **2017**, *29*, 5249–5258.
[76] J. Wang, K. Kovnir, *J. Am. Chem. Soc.* **2015**, *137*, 12474–12477.
[77] T. Caillat, J.-P. Fleurial, A. Borshchevsky, *J. Phys. Chem. Solids* **1997**, *58*, 1119–1125.
[78] G. J. Snyder, M. Christensen, E. Nishibori, T. Caillat, B. B. Iversen, *Nat. Mater.* **2004**, *3*, 458–463.
[79] J. H. Pohls, M. Heyberger, A. Mar, *J. Solid State Chem.* **2020**, *290*, 121557.
[80] M. A. White, G. J. Miller, J. Vela, *J. Am. Chem. Soc.* **2016**, *138*, 14574–14577.
[81] W. K. Hofmann, W. Jeitschko, *J. Less-Common Met.* **1988**, *138*, 313–322.
[82] W. Jeitschko, M. Reehuis, *J. Phys. Chem. Solids* **1987**, *48/7*, 667–673.
[83] V. Gvozdetskyi, V. Hlukhyy, R. Gladyshewskii, T. Fässler, *ZAAC* **2015**, *641*, 1859–1862.
[84] A. Z. Mewis, *Naturforsch. B* **1980**, *35*, 141–145.
[85] G. Brauer, E. Zintl, *Z. Phys. Chem.* **1937**, *(Abt. B)*, 37–323.
[86] K. J. Range, R. Ehrl, P. Hafner, *J. Alloys Compd.* **1996**, *240*, 19–24.
[87] H. J. Beister, K. Syassen, J. Klein, *Z. Naturforsch. B* **1990**, *45*, 1388–1392.
[88] X. Cheng, R. Li, D. Li, Y. Li, X.-Q. Chen, *Phys. Chem. Chem. Phys.* **2015**, *17*, 6933–6947.
[89] A. I. Shilov, K. S. Pervakov, V. A. Tafeenko, I. V. Morozov, *Russ. J. Coord. Chem.* **2020**, *46*, 622–630.

Manuscript received: June 2, 2021
Accepted manuscript online: September 1, 2021
Version of record online: October 12, 2021

